AGU PUBLICATIONS

JGR

Journal of Geophysical Research: Oceans

RESEARCH ARTICLE

10.1002/2015JC010990

Forcing and variability of nonstationary rip currents

J. W. Long[1] and H.T. Özkan-Haller[2]

[1]U.S. Geological Survey, St. Petersburg Coastal and Marine Science Center, St. Petersburg, Florida, USA, [2]College of Earth, Ocean, and Atmospheric Sciences, Oregon State University, Corvallis, Oregon, USA

Key Points:
- Four weeks of modeled neashore waves and currents over complex bathymetry
- Ratio of energy in each spectral peak dictates rip current characteristics
- Nonlinear advection affects number and location of rip currents

Correspondence to:
J. W. Long,
jwlong@usgs.gov

Citation:
Long, J. W., and H. T. Özkan-Haller (2016), Forcing and variability of nonstationary rip currents, *J. Geophys. Res. Oceans*, *121*, 520–539, doi:10.1002/2015JC010990.

Received 19 MAY 2015
Accepted 4 DEC 2015
Accepted article online 13 DEC 2015
Published online 14 JAN 2016

Abstract Surface wave transformation and the resulting nearshore circulation along a section of coast with strong alongshore bathymetric gradients outside the surf zone are modeled for a consecutive 4 week time period. The modeled hydrodynamics are compared to in situ measurements of waves and currents collected during the Nearshore Canyon Experiment and indicate that for the entire range of observed conditions, the model performance is similar to other studies along this stretch of coast. Strong alongshore wave height gradients generate rip currents that are observed by remote sensing data and predicted qualitatively well by the numerical model. Previous studies at this site have used idealized scenarios to link the rip current locations to undulations in the offshore bathymetry but do not explain the dichotomy between permanent offshore bathymetric features and intermittent rip current development. Model results from the month-long simulation are used to track the formation and location of rip currents using hourly statistics, and results show that the direction of the incoming wave energy strongly controls whether rip currents form. In particular, most of the offshore wave spectra were bimodal and we find that the ratio of energy contained in each mode dictates rip current development, and the alongshore rip current position is controlled by the incident wave period. Additionally, model simulations performed with and without updating the nearshore morphology yield no significant change in the accuracy of the predicted surf zone hydrodyanmics indicating that the large-scale offshore features (e.g., submarine canyon) predominately control the nearshore wave-circulation system.

1. Introduction

Rip currents are prominent features of nearshore circulation that are characterized by three main components: (1) converging feeder currents that flow parallel to the shoreline; (2) a rip "neck" consisting of a strong narrow jet directed offshore; and (3) an expanding rip head positioned outside of the surf zone where the flow begins to broaden [*Komar*, 1998]. The primary forcing for these flows has been well-studied and is generally thought to be the result of alongshore gradients in the incident wave height. While this general structure and forcing is consistent among observed rip currents, the mechanism responsible for the alongshore inhomogeneity in wave height and the temporal variability of rip currents can vary significantly. For a more comprehensive review of rip current dynamics and research, the reader is directed to *MacMahan et al.* [2006].

Many previous rip current studies have focused on flows that appear due to bathymetric variability in the surf zone. In particular, a depression or channel in an otherwise alongshore uniform sandbar can create a region of nonbreaking waves flanked on both sides by persistent wave breaking. The resulting alongshore pressure gradients force feeder currents to flow alongshore from both directions converging into an offshore-directed rip current which exits the surf zone through the channel. These rip currents are sometimes characterized as "fixed" or "topographic rips" and have been studied in both the laboratory [e.g., *Haller et al.*, 2002] and field [e.g., *Brander*, 1999; *MacMahan et al.*, 2004]. It has been shown that topographic rip currents are stronger and appear more often during low tide conditions [e.g., *Brander*, 1999] and that the position of the rip current is primarily fixed to the depressions in the bathymetry. Hence, changes in the rip current position occur on morphological time scales which, excluding discrete large wave events, are on the order of days and weeks or longer.

Rip currents have also been observed in nature to persist for much shorter-time scales and have been denoted in the literature as "transient rips" [*Johnson and Pattiaratchi*, 2004; *Smith and Largier*, 1995]. Multiple mechanisms with the ability to force these intermittent features have been previously identified. For

example, transient rips can be generated by spatial and temporal variations in the incident wave field that are associated with wave grouping [*Fowler and Dalrymple*, 1990; *Reniers et al*., 2004a] where the time scales of the rip current persistence are linked to the low-frequency time scales of the incident wave groups [*Long and Özkan-Haller*, 2009]. In general, topographic rip current locations mimic patterns in the nearshore bathymetry while transient rip current locations correspond to variability in the surface wave field and lack a preferential or persistent alongshore position. Both types of rip currents have some associated time variability. Topographic rip currents often exhibit pulsations about some persistent mean flow while transient rips exist for much shorter durations (O(1000 s)) which correspond to wave group time scales.

Long and Özkan-Haller [2005] discussed another type of rip current that is forced by strong alongshore wave height variations resulting from wave refraction over offshore bathymetric features (e.g., undulations in the walls of a submarine canyon observed during the Nearshore Canyon EXperiment, NCEX). They showed, using idealized conditions, that the number and location of predicted rip currents should be sensitive to characteristics of the offshore wave conditions. In this case, the temporal variability in persistence and location of rip currents will be linked to the time scale over which the offshore wave conditions change. This variability resides somewhere between that of the transient rip currents (O(1000 s)) and topographic rips (O(days-weeks)). Here we will use the term "non-stationary" rip currents in order to differentiate between this time scale and that of the transient rips studied by *Johnson and Pattiaratchi* [2004].

The goal of this work is to validate predictions of nonstationary rip currents that occurred over a 4 week period during NCEX and analyze the dynamics of the predicted rip currents. The aim here is twofold: (1) evaluate the efficacy of existing models to simulate nearshore hydrodynamics in alongshore nonuniform environments and (2) relate the spatial and temporal variations in rip currents that are difficult to resolve with field data to characteristics of the offshore wave field. In particular, we evaluate the relationship of rip location and strength with the wave and tidal conditions. Our analysis will be based on simulations of the wave and circulation fields during 28 consecutive days of the experiment. This provides 688 simulation hours for comparison to observations, in contrast to other studies that limit analysis to individual days/conditions [e.g., *Long and Özkan-Haller*, 2005; *Apotsos et al*., 2008a; *Hansen et al*., 2015].

We begin by describing the field experiment and numerical model in sections 2 and 3, respectively. Model results from the 4 week simulation are compared to both in situ and remote sensing observations in section 4. The definition and identification of the predicted rip currents and the relationship between the rip current dynamics and offshore wave conditions are described in section 5. A discussion regarding the influence of wave direction and nearshore bathymetry on the rip currents is given in section 6 followed by our conclusions in section 7.

2. Field Observations

The Nearshore Canyon Experiment (NCEX) was conducted in La Jolla, CA, during the fall of 2003. Extensive observations of nearshore hydrodynamics and morphodynamics in this highly complex coastal environment were collected over a 6 week time period. A deep offshore submarine canyon at the site is responsible for generating large alongshore gradients in wave height (factor of 4 change over 450 m alongshore distance) [*Apotsos et al*., 2008a] which drive substantial cross and alongshore currents.

2.1. Description of Nearshore Measurements

Properties of the nearshore hydrodynamics were recorded for the duration of the experiment with colocated pressure sensors and acoustic Doppler velocimeters (ADV) deployed primarily along the 1, 2.5, and 5 m isobaths. Additional pressure sensors and ADV's were located at 3 and 3.5 m water depths at one alongshore location just shoreward of the submarine canyon, and a pressure sensor was deployed in 15 m water depth at the northern end of the site (Figure 1). All instruments recorded data at 2 or 16 Hz for 51.2 min each hour [also see *Apotsos et al*., 2008a].

To estimate wave height in the nearshore, the power spectral density from the hourly pressure time series was found by averaging the periodograms computed from 11 overlapping (50%) 1024 point blocks with a cosine-shaped tapered window applied to each block. Linear water wave theory was employed to correct for depth attenuation at all wave frequencies. Pressure sensors deployed along the 1, 2.5, 3, and 3.5 m contours were buried beneath the seabed and the additional exponential attenuation of pressure through the sediment was accounted for following *Raubenheimer et al*. [1998]. Hourly estimates of significant

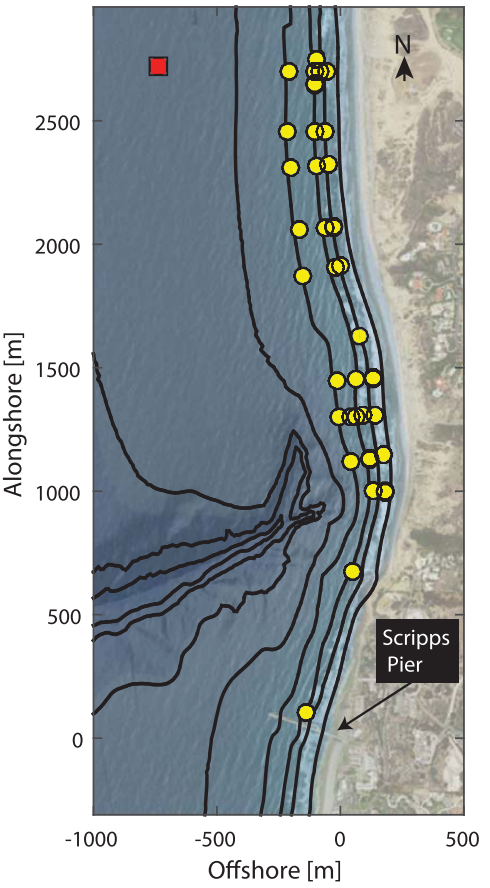

Figure 1. Locations of instruments deployed during the Nearshore Canyon Experiment (NCEX). The 0, 1, 2.5, 5, 10, 25, 50, 100 m depth contours are shown in black and the locations of the colocated pressure sensors and ADV's are indicated by the yellow circles. The red square represents the pressure sensor deployed in a water depth of 15 m.

wave height were then computed for each instrument as $H_s = 4 * \sqrt{mo}$ where *mo* represents the integrated power spectrum over a frequency range of 0.05–0.67 Hz.

ADV's were deployed along the curved coastline such that the measured cross and alongshore components of velocity were orthogonal to the local depth contour. The rotation of the instruments ranged between −15.9 and 21.6° with respect to true north depending on the alongshore location. The magnitude and direction of the hourly mean alongshore flows were computed by using averages over the 51.2 min time series for each instrument.

In addition to the hydrodynamic conditions, the nearshore bathymetry was measured approximately semi-weekly to observe the corresponding morphodynamic evolution. Surveys of the dry beach and inner surf zone were collected during low tide via an All-Terrain Vehicle (ATV) and human-powered push cart, respectively, both equipped with differential global positioning systems (GPS). Measurements of the mid and outer surf zone were recorded during high tide using personal watercraft equipped with an on-board sonar altimeter and differential GPS. The survey data spanned approximately 3 km along the coast and from the cliffs bordering the back of the beach to the 10 m depth contour. Previous measurements of the bathymetry over a larger domain including deeper water depths were available from multiple preexperiment sources [see *Long and Özkan-Haller*, 2005]. The merging of data to form the full map of the bathymetry used for numerical simulations will be addressed in section 3.

The in situ field measurements were complimented by video cameras imaging the same section of coast. The remote sensing images utilized as part of this study were collected during the first 10 min of each hour at a sampling rate of 1 Hz. These images provide a means to monitor rip current locations. The alongshore position of rip currents generated by a nearshore bar-channel system can usually be observed with video time exposure images through the light/dark contrast created by waves breaking over the sandbar (light) adjacent to the absence of wave breaking in the deeper channels (dark) [*Holman and Stanley*, 2007]. The rip currents considered here will not provide the same surface signature due to the lack of nearshore bathymetric depressions. Instead, the strong offshore flow will sometimes advect foam offshore and because this advection is time-dependent, a signal may show up best in the variance image (computed as the variance of all snapshots taken over a 10 min time period). Because the exact imaging mechanism of rip currents is unclear, a signal in the variance image indicates a rip is present, the lack of a signal not does ensure the opposite. In addition to the in situ observations, we use these remote sensing images as anecdotal evidence to further examine model performance.

2.2. Description of Offshore Wave Conditions

Offshore wave information was obtained every 30 min from the Outer Torrey Pines directional wave buoy (station 100; 550 m water depth) which is part of the network maintained by the Coastal Data Information Program operated by the Ocean Engineering Research Group (OERG) of the Integrative Oceanography Division (IOD) at Scripps Institution of Oceanography. The buoy is located approximately 7 miles offshore in a water depth of 550 m. Estimates of the directional wave spectra at the buoy are computed using the Maximum Entropy Method described in detail by *Lygre and Krogstad* [1986]. It was observed that many of the

spectra were bimodal with separate peaks corresponding to waves propagating from the northwest at ≈ 285° and from the southwest at ≈ 205° (nautical convention).

Over the 1 month period covered by the model simulations, the offshore wave conditions varied considerably. The range in wave conditions is given in Figure 2. Due to the persistence of bimodal spectra during the experiment, we have also identified the wave height, peak period, and peak direction of each spectral mode as well as the ratio of total energy between the northern and southern modes ($E_r = E_s/E_n$) (Table 1 and Figure 10). The time series can be separated into six regimes based on the relative importance of the two modes. From 1 to 6 October (regime I), the northern and southern peaks (average peak periods of 10.6 and 14.0 s, respectively), contained approximately equal energy. In the second regime (7–14 October), the wave field was dominated by waves propagating from the northwest with an average period of 10.6 s. During this time period, a 3 day storm occurred beginning on 9 October with wave height reaching a maximum of 1.7 m. The southern peak had similar characteristics to those observed during regime I. The spectra during regime IV (19–27 October) were similar to regime II except for the absence of the storm event.

Between regimes II and IV, the offshore wave spectra were dominated by waves propagating from the southwest (regime III, 15–18 October). During these 4.5 days, the average peak period of the southernwesterly waves was 14.0 s. Similar conditions occurred from 27 to 30 October (regime V). Finally, at the end of the month a 1 day storm occurred on 31 October with a maximum wave height of 1.4 m (regime VI). Unlike the longer duration storm that occurred earlier in the month, the average peak period of the dominant mode during this storm was only 7.4 s indicating a spectra characterized by northern wind seas rather than well-developed swell. A summary of the average wave conditions during each of the regimes is given in Table 1.

3. Model Description

Similar to *Gorrell et al*. [2011] and *Magne et al*. [2007], the nearshore transformation of waves over the submarine canyon is simulated using the SWAN wave model which solves the wave action balance equation [e.g., *Booij et al*., 1999]. For this work, we include the effects of wave refraction, shoaling, and depth-induced breaking and neglect nonlinear wave-wave interactions. Dissipation of wave energy through depth-induced wave breaking is included in the model using the parameterization of *Battjes and Janssen* [1978] with a constant breaking coefficient (γ) of 0.73.

A base bathymetry map including measurements of the offshore canyon was created by combining data collected during various preexperiment surveys [see *Long and Özkan-Haller*, 2005]. A chronological series of bathymetric maps were then assembled by updating the portions of the base map with nearshore survey data each time it was collected. Predictions of the wave transformation are made every 30 min, unless wave forcing information is not available at the offshore buoy. The wave model domain covers 10.75 km by 9.26 km and has a resolution of 10 and 15 m in the cross and alongshore directions, respectively, and is similar to that shown in *Long and Özkan-Haller* [2005]. The domain is oriented such that the x axis points east and the y axis points north and each model simulation utilizes the closest preceding bathymetric map. To account for tidally modulated water levels, the measured water level elevation obtained from a National Oceanic and Atmospheric Administration (NOAA) tide gage located close to the Scripps pier is uniformly added over the model domain for each 30 min simulation. The directional spectrum obtained from the offshore buoy is prescribed along the western offshore and northern lateral boundaries. Along the southern lateral boundary, the cross-shore variation of the incident spectra is approximated assuming refraction over straight and parallel contours. Simulations performed using either homogeneous or refracted spectra along the northern boundary yielded no discernible difference in the predicted wave heights within the NCEX experimental region.

To estimate the wave-induced nearshore circulation, we solve the phase averaged, depth-integrated Navier Stokes equations in a smaller region, nested inside the wave model domain. The model includes wave forcing computed from the radiation stress formulations by *Longuett-Higgins and Stewart* [1964] but neglects wave height variations over wave group time scales, includes horizontal momentum mixing, and a linear formulation for bottom friction [see *Long and Özkan-Haller*, 2005; *Özkan-Haller and Li*, 2003]. The friction coefficient was assumed to be temporally and spatially constant and assigned a value of 0.003 which is consistent with previous studies [*Apotsos et al*., 2008a; *Hansen et al*., 2015]. The tide is updated in the circulation

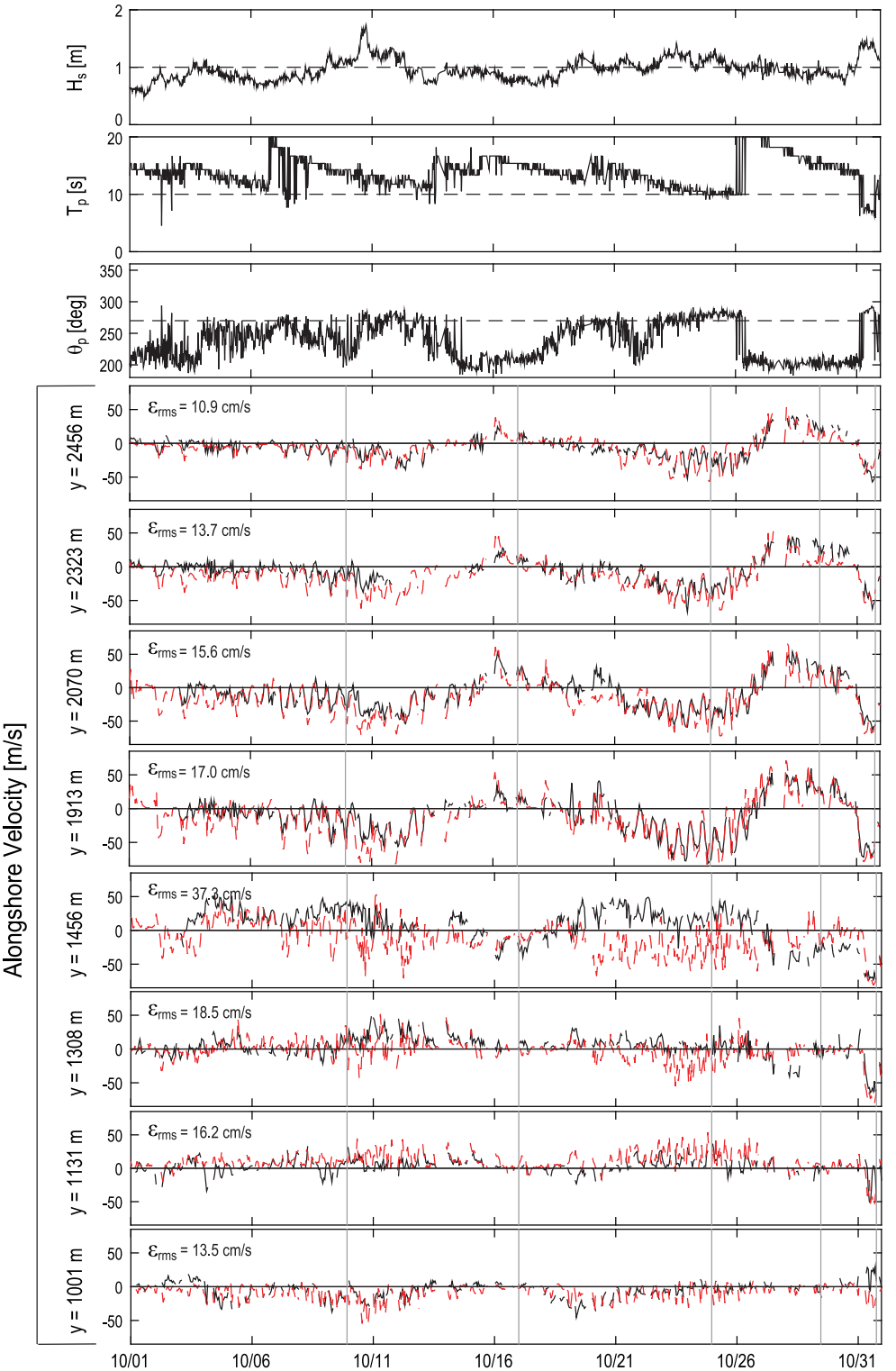

Figure 2. Offshore wave conditions during the month of October 2003 including significant wave height (H_s) with a reference line at 1 m, peak wave period (T_p) with a reference line at 10 s, and peak wave direction (θ_p) in nautical convention with a reference line at 270° in the top three subplots, respectively. Comparison of measured (black line) and modeled (red line) alongshore component of velocity at the ADV's deployed along the 1 m isobath. Alongshore position of the instruments is denoted on the *y* axis and the figure is oriented such that the individual plots progress from (top) north to (bottom) south (also see Figure 1). The root-mean-square error (ϵ_{rms}) is given for each individual time series. Gray lines denote the times corresponding to the case studies discussed in section 4.

Table 1. Directionally-Divided Offshore Wave Conditions: October 2003

		Northwestern Peak			Southwestern Peak		
Regime	E_r[a]	H_s[b] (m)	H_{max}[c] (m)	T_p[d] (s)	H_s (m)	H_{max} (m)	T_p (s)
I	1.03	0.52	0.82	10.6	0.49	0.74	14.0
II	0.53	0.78	1.50	10.6	0.53	0.75	14.4
III	2.68	0.42	0.68	9.2	0.63	0.89	14.0
IV	0.48	0.83	1.16	11.2	0.53	0.74	13.6
V	4.10	0.39	0.74	10.3	0.72	0.97	16.3
VI	0.41	1.04	1.22	7.4	0.64	0.76	13.1

[a]Ratio of wave energy between northern and southern spectral modes.
[b]Average significant wave height integrated over each spectral mode.
[c]Maximum significant wave height for each spectral mode.
[d]Average peak wave period for each spectral mode.

simulation every 10 min in order to maintain an accurate shoreline position. Upon updating the water depth, the position of the shoreline changes and a regridding of the model domain are required. For all simulations, the total number of cross-shore grid nodes is constant but they are redistributed in order to reach from the offshore boundary to the changing shoreline position. Radiation stress forcing provided by the wave model is updated every 30 min by gradually ramping from the previous to the new forcing values over approximately 2 min. A continuous 1 month circulation simulation is attempted but some brief interruptions occur when wave information is not available from the offshore buoy. Following an interruption, the circulation model is initiated from rest. The circulation model grid encompasses 650 m (offshore) by 2.5 km (alongshore) and has a spacing of 7.81 m in the alongshore direction and variable spacing in the cross-shore direction which changes with each regridding of the domain. On average, the cross-shore spacing is between 1.2 and 4.9 m with the highest resolution near the shoreline. The origin of the model domain is located at the Scripps pier and the cross-shore coordinate (x) increases onshore and points east while the alongshore coordinate (y) follows a right-handed coordinate system and points north (see Figure 1).

We only consider a one-way coupling between the wave and circulation models; hence wave radiation stress gradients that force nearshore flows are computed, but the effects of the currents on the incident wave field are neglected. While wave-current interactions are responsible for processes such as rip current pulsations and instabilities, they will not likely play an important role in the initiation, persistence, or migration of the rip currents over the longer time scales of interest herein. Instead, over the course of the 1 month simulation, variations in the offshore wave parameters, tide levels, and bathymetry will be of first-order importance in predicting the hourly to weekly rip current variability.

4. Model Performance

4.1. Wave Height

The semihourly modeled wave heights at each instrument location were averaged to compare with the measured hourly wave heights derived from the pressure sensors. Similar to *Gorrell et al*. [2011] and *Hansen et al*. [2015], the measured versus modeled wave height compare well with an average root-mean-square error ($\overline{\varepsilon_{rms}}$) of 11.6 cm and a model skill (S) of 0.86 computed using the method described by *Reniers et al*. [2004b] where

$$S = 1 - \frac{\sqrt{\frac{1}{N}\sum_{i=1}^{N}\left(\alpha_{m,i} - \alpha_{p,i}\right)^2}}{\sqrt{\frac{1}{N}\sum_{i=1}^{N}\alpha_{m,i}^2}}. \quad (1)$$

Here, α_m and α_p denote the measured and predicted quantities, respectively, and N is the number of observations in the total time series. Note that a skill level of unity would indicate a perfect prediction. A summary of the error statistics for instruments along each isobath is provided in Table 2. Notably, there is no significant difference between the model performance near to (skill = 0.84) and far from (skill = 0.88) the influence of the submarine canyon. The model error is largest at instruments along the 1 m isobath and

Table 2. Wave Model Error Statistics

	$y > 1500$ m				$y < 1500$ m			
Inst. Depth (m)	$\overline{\epsilon_{rms}}$ [a] (m)	$\bar{\epsilon}$ [b] (m)	m [c]	r^2 [d]	$\overline{\epsilon_{rms}}$ (m)	$\bar{\epsilon}$ (m)	m	r^2
1	0.13	−0.06	1.07	0.72	0.16	−0.07	1.12	0.73
2.5	0.10	−0.02	1.01	0.84	0.12	−0.04	1.03	0.86
5	0.10	−0.03	1.03	0.86	0.12	0.03	0.95	0.83

[a]Average root-mean-square error.
[b]Average mean error.
[c]Slope of the best-fit line from a linear regression.
[d]Squared correlation coefficient.

tends to overpredict the wave height at all alongshore locations at that isobath but does reproduce the observed monthly and tidal trends.

In these simulations, none of the free parameters in the wave or circulation models have been calibrated. We did, however, run three 24 h wave simulations (144 individual model runs) that used a lower constant wave breaking coefficient (γ) of 0.6 and another set of simulations using the expression for γ as a function of offshore wave height derived by *Apotsos et al.* [2008b] to assess the model sensitivity to the wave breaking coefficient. The 3 days considered covered the range of wave conditions observed during the experiment and while better agreement with the observations was achieved for a few individual hours at some alongshore locations, the average error statistics at all instruments were not improved.

4.2. Alongshore Velocity

Unlike cross-shore currents, alongshore flows have been shown to be approximately depth-uniform, meaning that a single point measurement in the water column would be representative of a depth-integrated flow similar to what the model predicts [*Reniers et al.*, 2004b]. Hourly statistics of the alongshore component of velocity (rotated to be locally orthogonal to the curved coastline) predicted by the model and interpolated to the instrument locations are obtained by neglecting the first 10 min after each wave forcing update (half hour intervals) and averaging the remaining 40 min of simulation time. Comparison to the observed mean alongshore current along the 1 m isobath is shown in Figure 2. We note that during times when the instruments along deeper isobaths (2.5 and 5 m) were within the surf zone, the agreement between the model and data is similar to that presented here. Variations attributed to the changing tide are evident in both the predicted and observed currents. There are also longer-term changes in the direction of the current at each instrument that are related to changes in offshore wave energy and peak direction. The ε_{rms} for instruments along the 1 m isobath ranged between 11 and 37 cm/s with an average of 17.8 cm/s. While seven of the instruments had an ε_{rms} that ranged between 11 and 18.5 cm/s, there is notably one location just north of the canyon head where the model poorly represents the observed flow (Figure 2; fifth subplot from top) for more than half of the time series ($\varepsilon_{rms} = 37.2$ cm/s).

We investigated a number of possible explanations for this disagreement. Increasing the cross-shore model resolution by a factor of 3 yielded no significant changes in the predicted wave transformation or corresponding circulation. Additionally we found that the surf zone width observed in remote sensing images was predicted well. We also verified that the model bathymetry around the instrument corresponded to both the surveyed water depths and the depth measured by the altimeter. Finally, we compared two 5 day simulations performed with and without wave-current interaction terms. In those simulations, the $\overline{\varepsilon_{rms}}$ in alongshore velocity at the 1 m instrument array was 18 cm/s (17 cm/s) when excluding (including) wave current-interaction. Nonetheless, the our overall model performance (average r^2 north (south) of the canyon = 0.69 (0.16)) is similar to that of *Hansen et al.* [2015] for the same region (average r^2 north (south) of the canyon = 0.59 (0.22)).

4.3. Case Studies

4.3.1. Northwestern Wave Incidence

To further validate model performance and explore the range of conditions, we discuss a series of case studies for which video observations and in situ data were both available. An example of the nearshore wave and circulation field that arises under predominately northwestern wave incidence (9 October 2003 2200 GMT (regime II)) is shown in Figure 3. Near the northern edge of the model domain, away from the

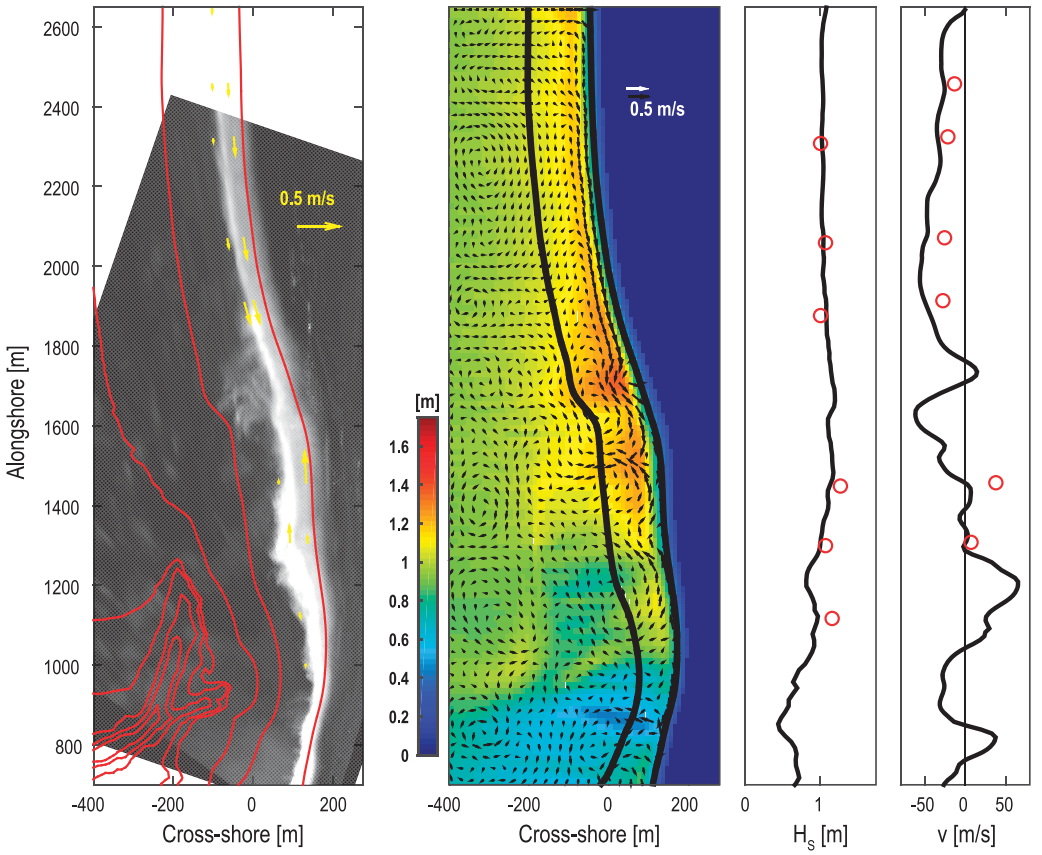

Figure 3. Predicted and observed nearshore hydrodynamics for 9 October 2003 at 2200 GMT. Depth contours (1,5,10,20,25,35,50,75,100 m) are superimposed on the Argus variance image (first plot) along with yellow vectors denoting the measured alongshore current velocity at the instrument locations. The model predicted wave height (colormap) and circulation vectors are shown in the second plot where the bold lines denote the alongshore transects used for model-data comparisons of wave height (seaward line) and alongshore velocity (shoreward line) which are shown in the third and fourth plots, respectively.

influence of the canyon, the radiation stress forcing causes a southward directed alongshore current. Closer to the submarine canyon, wave refraction causes focusing of wave energy just north of Scripps canyon and the southward alongshore current is modified by the associated alongshore gradients in wave setup often resulting in a rip current ($y \approx 1700$ m). Wave height comparisons with in situ observations along the 5 m isobath show good agreement with $\overline{\varepsilon_{rms}} = 12.4$ cm. The alongshore current predictions inside the surf zone at the 1 m isobath follow the observed trends ($\overline{\varepsilon_{rms}} = 23.0$ cm/s) although some discrepancies at individual instruments do exist.

The observed variance image in Figure 3 (left) indicates the presence of a rip current at $y \approx 1650$ m which is supported by the appearance of a convergence in the alongshore current measured by the in situ data. An offshore flow at the same alongshore position is also present in the modeled circulation, however, an even stronger offshore flow is predicted slightly to the south at $y \approx 1500$ m. It is unclear whether the modeled alongshore rip current position is biased slightly to the south or if this is a second rip current that did not provide a separate surface signature. Another rip current at $y \approx 850$ m is observed in the model in a region not instrumented with in situ devices and not apparent in the video image.

A variance image from another rip current event (regime IV), along with the predicted circulation is shown in Figure 4. In the northern part of the domain ($y > 1500$ m), both the model and data indicate the presence of a southward directed alongshore current. There is a small area of wave focusing present at about $y = 1700$ m that causes the modeled alongshore current to turn slightly offshore. For $y < 1500$ m, the wave height patterns become much more nonuniform, similar to the previous example case. A rip current is identified in the image at about $y = 1350$ m and the model is able to predict its presence. Overall, good agreement is obtained for both wave height ($\overline{\varepsilon_{rms}} = 10.8$ cm) and alongshore velocity ($\overline{\varepsilon_{rms}} = 24.6$ cm/s).

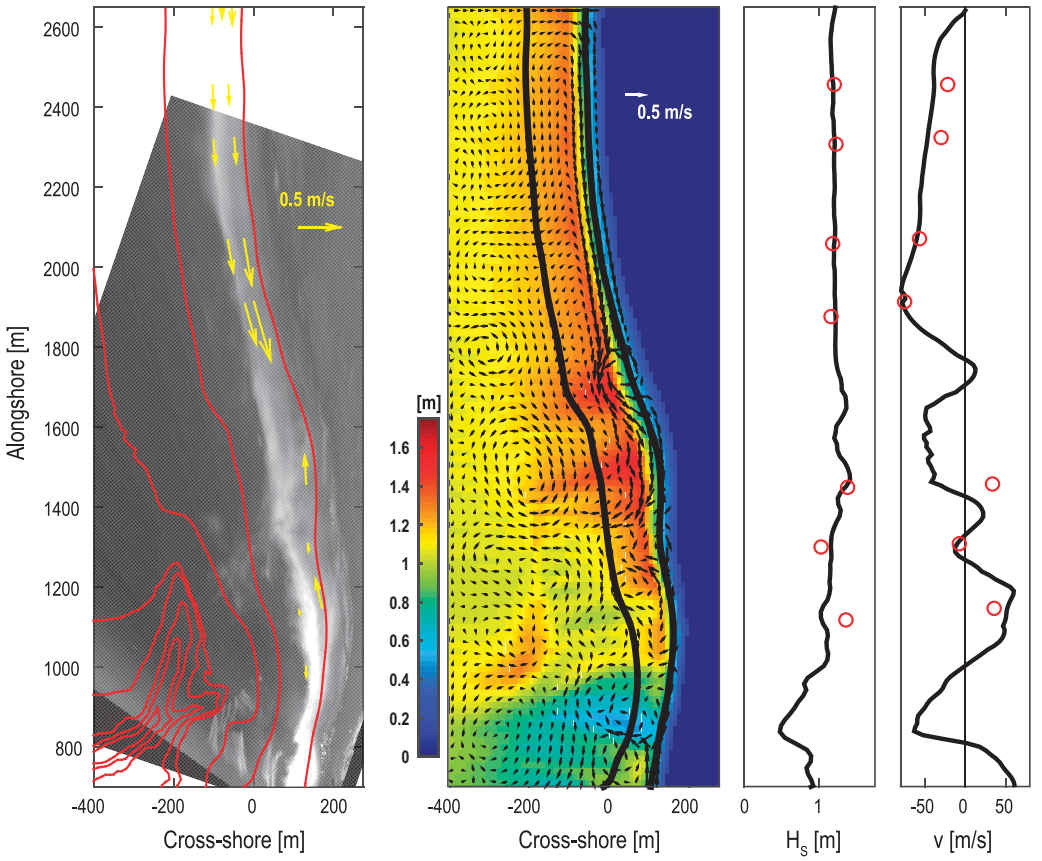

Figure 4. Predicted and observed nearshore hydrodynamics for 25 October 2003 at 0000 GMT. Depth contours (1,5,10,20,25,35,50,75,100 m) are superimposed on the Argus variance image (first plot) along with yellow vectors denoting the measured alongshore current velocity at the instrument locations. The model predicted wave height (colormap) and circulation vectors are shown in the second plot where the bold lines denote the alongshore transects used for model-data comparisons of wave height (seaward line) and alongshore velocity (shoreward line) which are shown in the third and fourth plots, respectively.

An example of the influence of incident wave period on the circulation patterns can be discerned in the rip current locations during regime VI when the average peak period decreased to 7.4 s (Figure 5). Here, both the measured and modeled velocities show a southward alongshore current over much of the region (wave height $\overline{\varepsilon_{rms}} = 12.2$ cm; alongshore velocity $\overline{\varepsilon_{rms}} = 15.2$ cm/s). At the far southern portion of the domain, the variance image indicates a rip current at $y = 1000$ m, and a corresponding oblique offshore flow is present in the model simulations. Under these conditions, the waves are less affected by the offshore bathymetric features and a more uniform wave height distribution develops in the nearshore.

4.3.2. Southwestern Wave Incidence

Waves approaching from the southwest dominated the offshore spectrum on 29 October 2003 at 1200 GMT (regime V) and the observed and simulated nearshore hydrodynamics are shown in Figure 6. Similar to the previous case, wave energy focuses in the region just north of the canyon head but a rip current north of the focus region ($y = 1750$ m) does not develop because both the radiation stress gradients and the pressure gradient-induced flow force a positive (northward) alongshore current. A prominent shadow region in the lee of and south of the canyon exists under this scenario creating a strong alongshore wave height gradient south of the canyon ($y < 1500$ m). The modeled wave height compares well with in situ observations $\overline{\varepsilon_{rms}} = 7.5$ cm) and shows a reduction in significant wave height of up to 50% over approximately 300 m which is consistent with the description by *Apotsos et al.* [2008a]. The resulting modeled flow is characterized by an onshore flow over the wave focusing region, diverging alongshore currents in the surf zone at that alongshore position ($y = 1600\,m$), and occasional rip currents occurring to the south. The modeled alongshore currents are consistent with existing observations ($\overline{\varepsilon_{rms}} = 7.5$ cm/s). Data from other days with similar wave conditions also clearly show the divergent nature of the alongshore flow. Note that the alongshore momentum balances modeled and analyzed from in situ measurements by *Apotsos et al.* [2008a] all

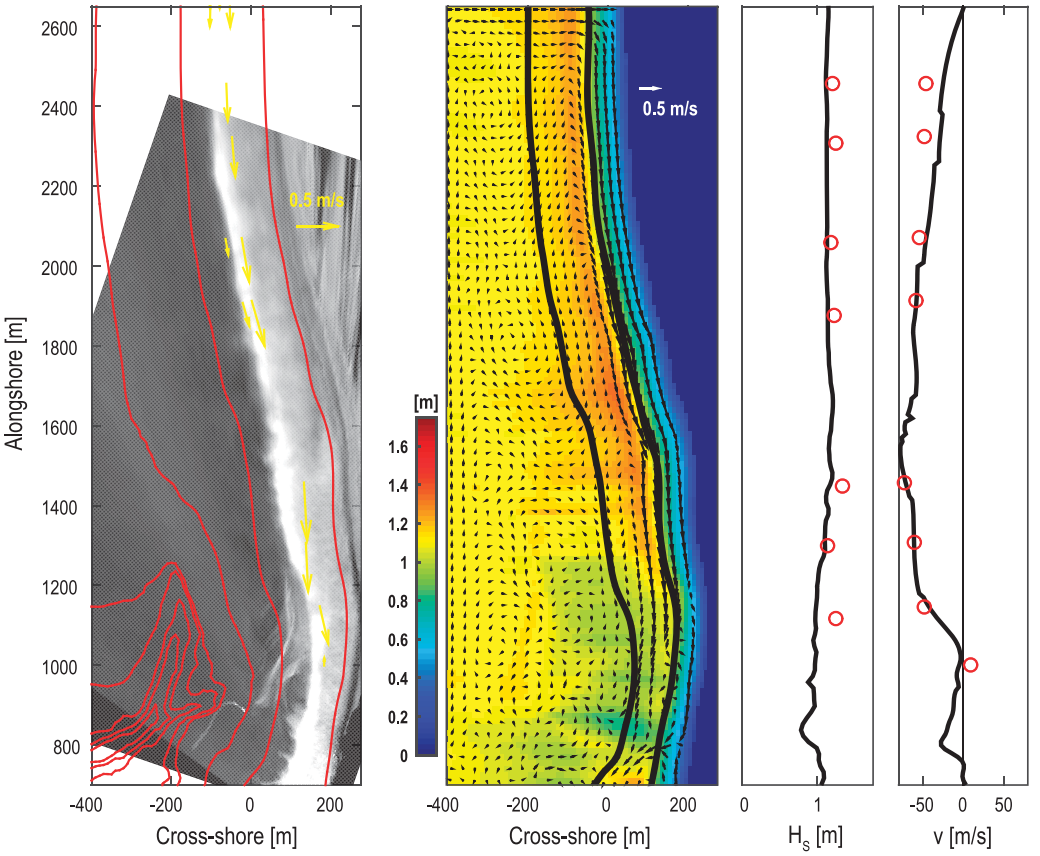

Figure 5. Predicted and observed nearshore hydrodynamics for 31 October 2003 at 1800 GMT. Depth contours (1,5,10,20,25,35,50,75,100 m) are superimposed on the Argus variance image first plot) along with yellow vectors denoting the measured alongshore current velocity at the instrument locations. The model predicted wave height (colormap) and circulation vectors are shown in the second plot where the bold lines denote the alongshore transects used for model-data comparisons of wave height (seaward line) and alongshore velocity (shoreward line) which are shown in the third and fourth plots, respectively.

fall into time periods where the southern spectral mode was dominant, and this strong alongshore wave height gradient south of the canyon existed.

Another example when southwesterly waves dominated the offshore incident spectrum is shown in Figure 7 (regime III). The velocity vectors obtained from the in situ measurements and model both show a divergence in the alongshore current at about $y=$ 1700 m due to a region of wave focusing at that location. The patterns of wave focusing for this time period are similar to those shown above for 29 October but are less energetic. The flows under these wave conditions are weak and the model produces the general alongshore trends in both wave height ($\overline{\varepsilon_{rms}}$=6.2 cm) and alongshore velocity ($\overline{\varepsilon_{rms}}$=13.2 cm/s). Although the model shows an indication of small offshore directed flow in some areas, they are not likely to be identified as rip currents in our analysis or expected to strongly advect foam offshore and appear in the remote sensing images.

Overall, despite the complex nature of the bathymetry and wave height patterns at this site, the error statistics are similar to those of previous studies [*Gorrell et al.*, 2011; *Hansen et al.*, 2015]. In our case, the model-data comparisons suggest the model can accurately predict the observed wave height ($\overline{\varepsilon_{rms}} < 12$ cm) and alongshore currents ($\overline{\varepsilon_{rms}}$ generally < 20 cm/s) over the daily and weekly time scales of interest. In addition, the direction of the alongshore current is predicted correctly 82% of the time (excluding observed flows < 10 cm/s). If the instrument located at y=1458 m is excluded from the analysis, the prediction accuracy increases to 86%. This suggests the convergences/divergences of the alongshore flow, and therefore the existence of rip currents, will be captured. Moreover, when rip currents are clearly visible in the remote sensing images we obtain qualitative agreement between the modeled and observed alongshore rip current locations.

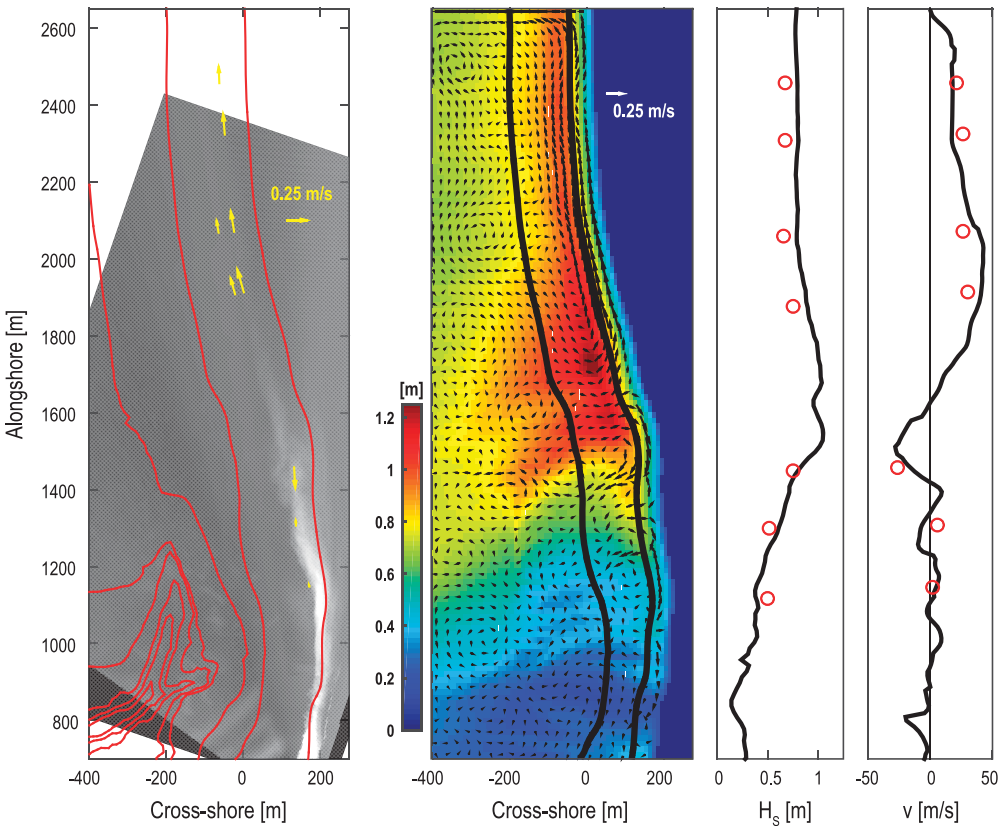

Figure 6. Predicted and observed nearshore hydrodynamics for 29 October 2003 at 1200 GMT. Depth contours (1,5,10,20,25,35,50,75,100 m) are superimposed on the Argus variance image (first plot) along with yellow vectors denoting the measured alongshore current velocity at the instrument locations. The model predicted wave height (colormap) and circulation vectors are shown in the second plot where the bold lines denote the alongshore transects used for model-data comparisons of wave height (seaward line) and alongshore velocity (shoreward line) which are shown in the third and fourth plots, respectively.

5. Rip Current Dynamics

5.1. Rip Current Identification

In order to track the formation, location, and persistence of rip currents predicted by the model we identify them using a threshold for the cross-shore velocity exiting the seaward edge of the surf zone. The offshore surf zone boundary is identified for each hour as the most seaward location where the fraction of breaking waves computed in the wave model is greater than 0.01. This value was found to correspond qualitatively to the cross-shore location of the most seaward band of light intensity observed in the remote sensing variance image. This seaward band of high variance appears in the remote sensing data due to the intermittent breaking of only the largest waves. The hourly averaged cross-shore velocity from the circulation model is then interpolated to this surf zone boundary.

We use two criteria to define a rip current. The first criterion required that the cross-shore component of flow (orthogonal to the local depth contour) exiting the surf zone be at least greater than 10 cm/s. Our second criterion is that the cross-shore component of flow must be larger than the alongshore component at the same location. These criteria were found to eliminate meandering alongshore flows with weaker cross-shore velocities. Using these definitions, we identify the alongshore position of any predicted rip currents in the domain each hour of the total simulation. The strength of the rip current is defined as the magnitude of the cross-shore velocity exiting the surf zone at those alongshore positions.

5.2. Rip Current Position

The spatial and temporal variability of the modeled circulation patterns previously discussed show that the predicted rip currents will display changes in magnitude and alongshore position throughout the month. In fact, an analysis of the rip current locations as a function of time reveals notable variability in alongshore rip

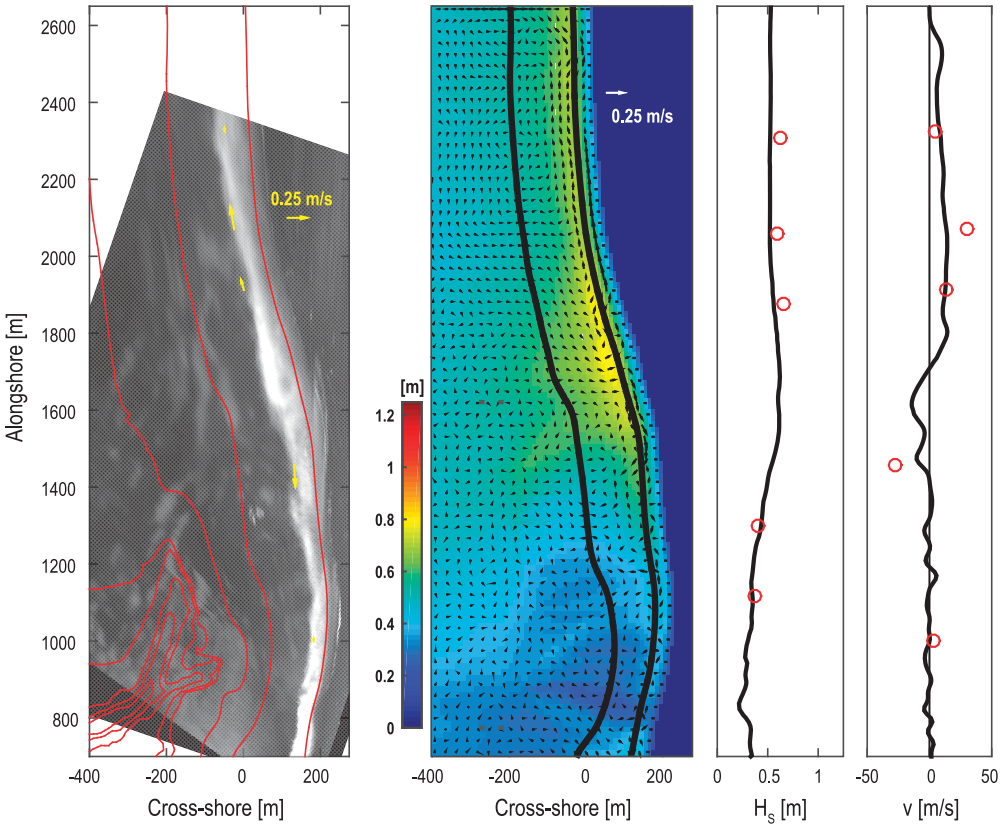

Figure 7. Predicted and observed nearshore hydrodynamics for 17 October 2003 at 0000 GMT. Depth contours (1,5,10,20,25,35,50,75,100 m) are superimposed on the Argus variance image (first plot) along with yellow vectors denoting the measured alongshore current velocity at the instrument locations. The model predicted wave height (colormap) and circulation vectors are shown in the second plot where the bold lines denote the alongshore transects used for model-data comparisons of wave height (seaward line) and alongshore velocity (shoreward line) which are shown in the third and fourth plots, respectively.

current position and strength on even hourly time scales (Figure 8). Rip currents tend to preferentially occur in four general regions near $y = 845$ m, 1231 m, 1485 m, and 1817 m, although the precise alongshore position of the rips in these regions varies by as much as 200 m.

The rip current near $y = 845$ m is relatively stationary (maximum standard deviation in the alongshore position of 33 m), and appears consistently when waves from the northwest are dominant ($E_r < 1$). At the end of regimes II and IV, when southwestern waves gain prominence, this rip current migrates north, weakens and disappears rapidly. The rip current near $y = 1231$ m exists during most of the month of October regardless of incident wave conditions. It is also relatively stationary (standard deviation in position of 42 m), except for a short period of time during regimes I and VI when it rapidly migrates southward by as much as 200 m. This migration coincides with a time when the waves from the northwest have shorter wave periods ($T \approx 7$ s), and the southward alongshore current magnitude increases (see also Figure 2, $y = 1458$ m). A similar rapid southward migration of about 200 m can also be observed in the rip current centered around $y = 1485$ m. This rip also exists during the entire month, but the position of this rip is generally more variable (standard deviation of 107 m), most notably during regimes II and IV, when the rip position oscillates between two locations (near $y = 1600$ m and 1400 m) at tidal time scales (also see Figure 9). This tidal oscillation in position will be discussed further below. Finally, the rip current centered around $y = 1817$ m is located just to the north of Scripps Canyon, a location where wave focusing was often observed. It is primarily present when waves from the northwest dominate ($E_r < 1$) because it is formed when the southward directed alongshore current (driven by the wave forcing) encounters an opposing pressure gradient forced flow caused by wave focusing to the north of the canyon tip. This rip current shows a pronounced southward migration and weakening during regime IV, followed by a rapid northward migration, further weakening and disappearance as waves from the southwest become more prominent at the beginning of regime V.

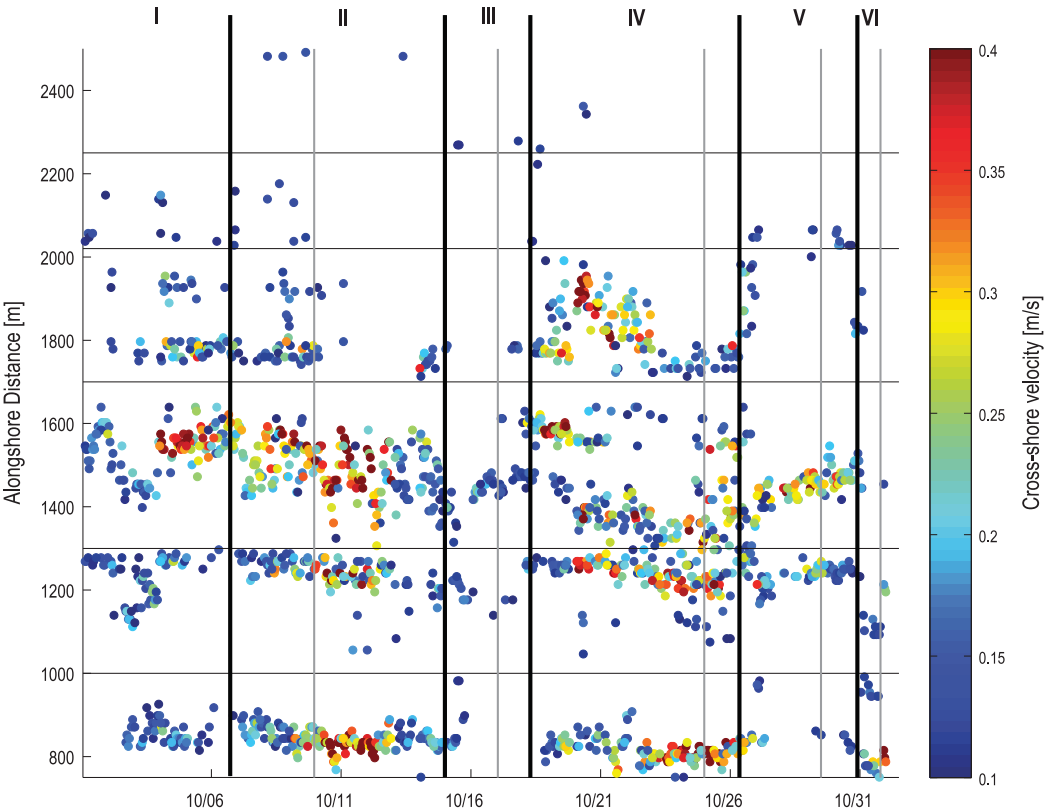

Figure 8. Rip current position versus time as predicted during the 4 week model simulation. The strength of the rip current is denoted according to the color of the individual dots. Horizontal black lines indicate the alongshore bins used to separate the rip currents for further analysis and the gray vertical lines denote the times corresponding to the case studies discussed in section 4. The bold vertical lines separate the experiment into six regimes discussed throughout the text.

Using a linear and nonlinear model for a series of idealized cases, *Long and Özkan-Haller* [2005] showed that nonlinear inertial effects associated with the alongshore current played an important role in dictating the alongshore rip current position, causing an alongshore shift in the rip current location compared to a linear model result. They also showed that the inertia of the alongshore current could be important enough to overcome surf zone setup gradients and prevent the occurrence of a rip current even if wave and setup gradients were conducive of the existence of a rip. Recently, through analysis of alongshore momentum balances on one day of the experiment, *Hansen et al*. [2015] concluded that scatter observed in field-derived momentum balances was largely attributed to unresolved nonlinearity. To determine the effect of nonlinearity for this month-long simulation, we used the linearized model described in *Long and Özkan-Haller* [2005] which neglects nonlinear advective terms in the momentum balance and simulated the entire month-long time series. We compared the cross-shore integrated bottom friction term in the time-averaged alongshore momentum balance computed from original and linearized models to determine the effect on rip current generation and position. Note also that the model utilized a linear friction term, and alongshore variability in the friction term is primarily due to variability in the alongshore current itself.

We concentrate on a period of time centered around regime IV when model results indicate large changes in the position of the northernmost rip current ($y = 1817$ m). Our objective is to discern if these changes are directly forced by changes in the incident wave field at those time scales (in which case the linear model results will show changes in the feeder current patterns) or if nonlinear advection plays a role. Figure 9 shows the cross-shore integrated bottom friction term from the nonlinear model during regime IV. Changes in sign of the bottom friction term indicate convergences (going from green to red with increasing alongshore distance) and divergences (going from red to green with increasing alongshore distance) in the alongshore current, and the locations of convergences can be interpreted as rip currents. Note that rip currents can also form in the absence of opposing feeder currents if the alongshore gradient in the alongshore

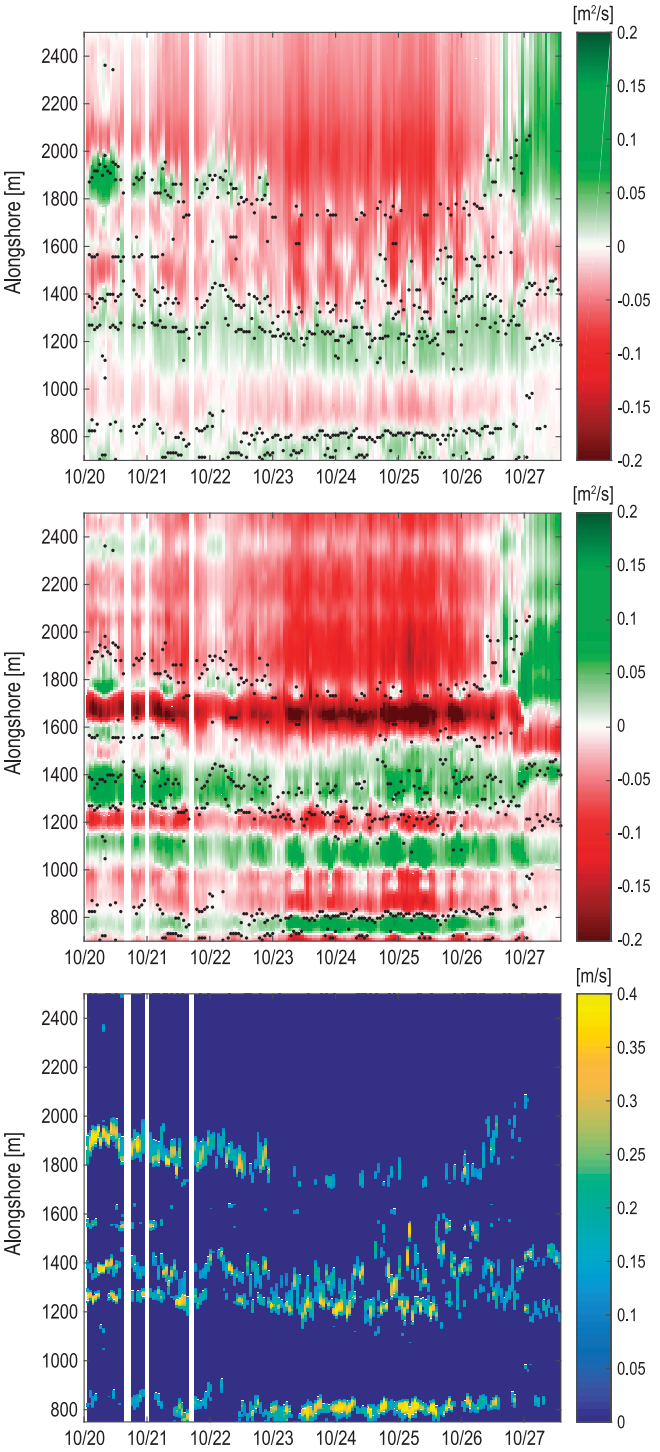

Figure 9. Cross shore integrated bottom friction term in the time-averaged alongshore momentum balance from the (top) nonlinear and (middle) linear model as a function of time and alongshore position during regime IV. The black dots indicate the alongshore position of modeled rip currents at the outer edge of the surf zone from each respective model. (bottom) Cross-shore rip current velocity at the outer edge of the surf zone from the nonlinear model.

current (and the associated cross-shore gradient in the cross-shore current) is large. In this case, the rip current would tend to be highly oblique.

Figure 9 starts on 20 October, when waves approaching from the northwest begin to dominate (see Figure 10). Far north of the canyon ($y > 1600$ m), an alongshore current toward the south is generated due to the incident wave angle. By 21 October, the southward alongshore current is well-established, but has yet to gain significant strength (also see observations in Figure 2) and a rip current exists near $y = 1900$ m. Comparison of the convergences predicted by the linear and nonlinearmodel simulations (compare the transition from green to red between top and middle plots of Figure 9) indicate that the location of the this rip is displaced southward by approximately 100 m due to nonlinear advection. Starting on 22 October, the waves from the northwest and the associated southward mean alongshore current strengthen and persist for 4 days. During the first 24 h of this period, some tidal oscillations in the alongshore convergence location are evident. These oscillations are primarily related to changes in the surf zone bathymetry as the shoreline position shifts with the changing tide. Both the linear and nonlinear model indicate an alongshore shift in the predicted rip location, but the nonlinear model also shows that by 23 October the zero crossing in the alongshore (feeder) currents is eliminated by the effects of nonlinear advection. Consequently, the rip current moves rapidly southward, is significantly weakened, and the flow pattern resembles an undulating alongshore current rather than a rip current system (see Figure 4, around $y = 1800$ m).

Figure 9 also suggests that the rip current near $y = 1485$ m is significantly affected by nonlinear advection. Moreover, it displays the strongest tidal variation in its feeder currents (and hence its position). The position of the remaining rips are also affected by up to 75 m. At the end of regime IV, the wave angle of incidence switches and the alongshore current north of the canyon turn toward the north. The rip current near $y = 1817$ m rapidly moves northward and eventually

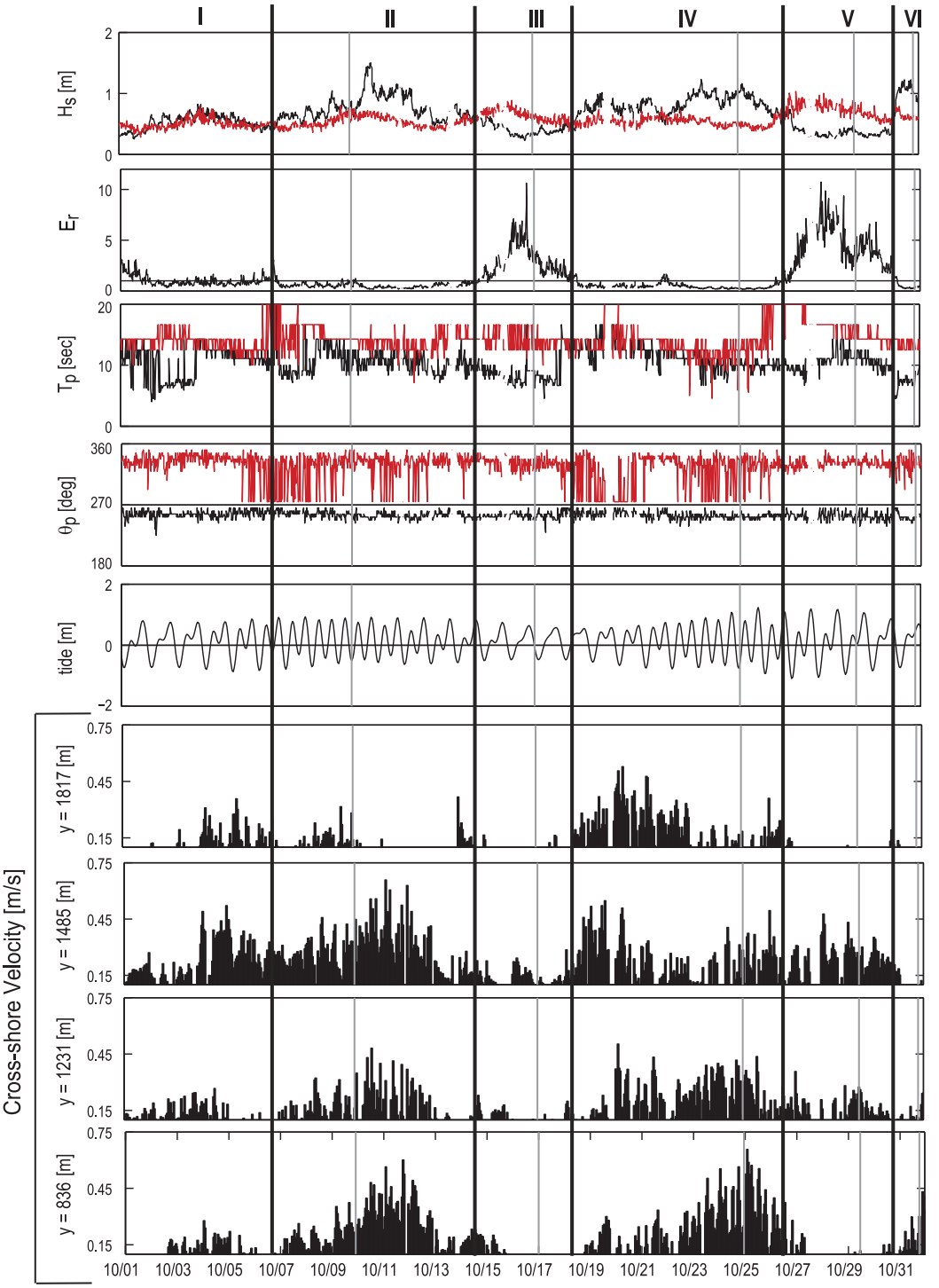

Figure 10. Time series of the observed significant wave height (m) (first plot) for waves approaching from the North (black) and South (red), energy ratio between southern and northern wave modes ($E_r = E_S/E_N$) with a reference line at $E_r = 1$; peak wave period (s) (second plot), peak wave direction (°) (third plot) with a reference line at shore normal wave incidence. Angles above(below) this line are waves approaching from the north(south). The fourth plot is the recorded tide level variations (m). The bottom four plots represent rip current velocity time series in the four southernmost alongshore bins denoted in Figure 8 where the height of the bar indicates the magnitude of the rip current (m/s) at the seaward surf zone boundary. The mean positions of the rip currents are denoted on the *y* axis. Black vertical lines separate the time series into the six regimes discussed throughout and the light gray lines denote the times corresponding to the case studies discussed in section 4.

disappears. Although we only show a small portion of the model simulations, substantial differences in both rip current existence and location exist during all regimes when comparing the nonlinear model with the linear estimate, suggesting that inertia plays an important role in the rip current dynamics at this site. We also note that data-model comparisons using the linear model show a marked decrease in skill. The error increased at all instruments with $\overline{\varepsilon_{rms}}$ increasing from 17.8 cm/s (nonlinear model) to 30.2 cm/s (linear model).

5.3. Rip Current Strength

By separating the domain into six alongshore bins, month-long time series of the rip current magnitude are generated for further analysis. When more than rip current is present in the same alongshore bin, the maximum velocity is used. Given the previous evidence indicating that these rip currents are controlled by the refraction patterns of the incident waves over the offshore bathymetry, we seek to relate the time series of cross-shore flow to the parameters of the offshore wave field. Also, previous research has shown that the presence and strength of rip currents forced by alongshore variations in the nearshore bathymetry are strongly influenced by changes in tidal amplitude [e.g., *Brander*, 1999; *MacMahan et al*., 2005]. It is unclear, from the literature, what effect the tide has on rip current strength when they are controlled by offshore bathymetry.

The four alongshore bins displaying the most rip current activity are shown in Figure 10, along with the observed range in incident wave conditions. We find that rip current strength is highly variable and can reach up to 65 cm/s. The rip current near $y = 1485$ m is overall the strongest and most persistent rip current. Aside from the rip current at $y = 1817$ m, an increase in rip current strength is linked to increases in the offshore wave height with statistically significant r^2 values of up to 0.51 for certain time periods. However, at times inertial effects related to strong alongshore currents generated during large wave events can affect the rip currents and weaken them (e.g., toward the end of regime IV or regime VI). In contrast to studies of topographic rips, a linear regression analysis between the time series of rip current magnitude and the record of tidal elevation shows no significant correlation ($r^2 < 0.1$ for all rips).

6. Discussion

6.1. Dependence on Wave Direction

The existence and strength of rip currents at this site are strongly tied to the nature of the incident wave field. When northern swell waves are dominant (regimes I, II, and IV), the refraction patterns are conducive to rip currents throughout the domain. A histogram of the number of rip currents present during these times indicates that an average of 3 rip currents were predicted in the model domain. The last day of the month (regime VI), the wave conditions shifted to locally generated wind seas rather than the well-developed swell waves observed during the other regimes. As described by *Long and Özkan-Haller* [2005] for a series of idealized cases, short period incident waves will be less affected by variations in the bathymetry at deep water depths, hence the alongshore wave height variability in the surf zone is decreased. This, in addition to the inertia of the alongshore current that can overcome small alongshore pressure gradients, results in the generation of very few rip currents in the domain. Those that do appear are concentrated in the southern portion of the domain. These effects are evident because rip currents are concentrated in only the southernmost alongshore bins in Figures 8 and 10. In contrast to the northern wave conditions, regimes III and V are dominated by waves approaching from the southwest. During regime III, the number and relative magnitude of rip currents in the domain decreases and the majority of rip currents that are identified have a magnitude less than 20 cm/s. To better assess this directional dependence, idealized simulations were designed to vary the ratio of northern to southern wave energy contained in the spectrum and evaluate changes that occur in the wave and circulation fields.

The bathymetry measured at the beginning of the experiment and a series of idealized TMA spectra were used for each simulation [*Bouws et al*., 1985]. As a baseline, the first two simulations correspond to single mode spectra with waves approaching from either northwestern or southwestern wave directions (Figure 11). The peak wave frequency, direction, and the widths in both frequency and direction were chosen such that they correspond to those observed during the experiment. Characteristics of the idealized incident spectra are given in Table 3. We note here that the northwestern waves usually approach from around 15° from shore normal (270°) while the southwestern waves are much more oblique at 60–70° from

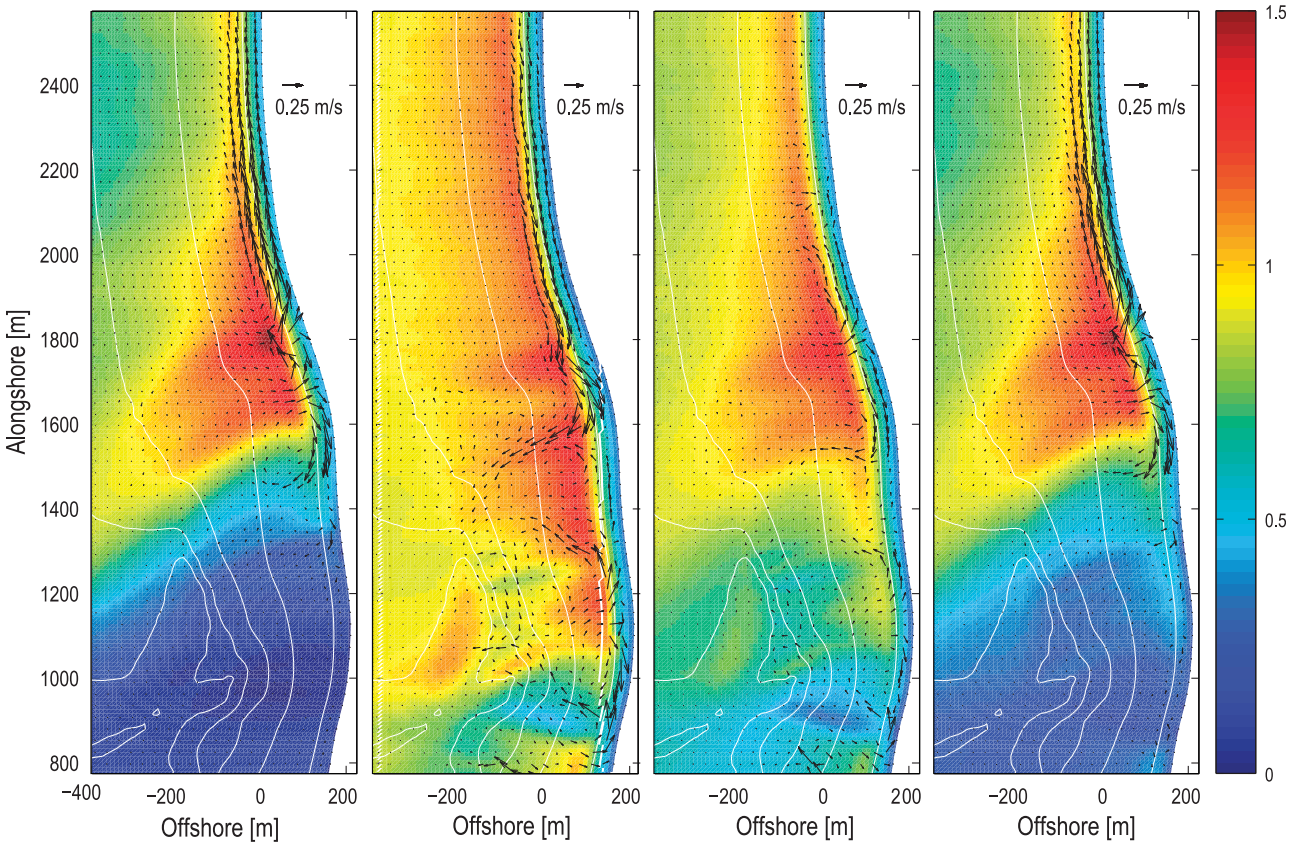

Figure 11. Wave height (color scale) and circulation (black vectors) model results using measured bathymetry and a series of idealized spectra including an energy peak from the south (left), an energy peak from the north (middle-left), equal energy between the northern and southern peaks ($E_r = 1$)(middle-right), and three times more energy in the southern peak than the northern peak ($E_r = 3$)(right).

shore normal. Comparison of the nearshore wave field for these two simulations reveals that under southern wave conditions, the smaller scale (O(100 m)) alongshore wave height variations are much less pronounced and therefore multiple rip currents do not develop (Figure 11; first and second plots).

Maintaining the same characteristics of the spectral peaks used above, we also initiated the model with idealized bimodal spectra and varied the relative strength of each mode. When the energy ratio (E_r) is unity, the wave field still displays some smaller-scale variability at $y < 1400$ m but resembles results from the southern wave condition at $y > 1400$ m (Figure 11; third plot). The mean alongshore current north of the canyon ($y = 2400$ m) is minimal. As the energy ratio becomes larger, the southern peak dominates and the small-scale alongshore wave height variability decreases (Figure 11; fourth plot). Not surprisingly, this causes a subsequent decrease in rip current activity (number and magnitude) which is evident in the flow fields.

Table 3. Parameters for Idealized TMA Wave Spectra

Spectral Mode	θ_p (°)[a]	f_p (Hz)[b]	nn[c]	γ[d]
Northwestern	285	0.11	10	15
Southwestern	195	0.065	200	65

[a]Peak wave direction.
[b]Peak wave frequency.
[c]Directional spreading coefficient where the directional width the spectrum is proportional to cos^{nn}.
[d]Spectral peakedness parameter that dictates the width of the frequency spectrum.

6.2. Dependence on Nearshore Bathymetry

During the course of the month, the nearshore bathymetry evolved, and although prominent rip channels were not observed, there were changes of up to 50 cm in depth between surveys. To assess the relative importance of these bathymetric changes in controlling the rip current dynamics, we repeated the model simulation using the bathymetry measured at the beginning of the month for the entire length of the simulation. The wave height $\overline{\epsilon_{rms}}$ at the 1 m instrument array (location of greatest error in

previous model run) for this simulation was only 0.26 cm greater than the error in the previous simulation (<2% increase in error). Similarly, the error in the circulation model performance at the 1 m instrument array increased on average by 1.23 cm/s (7% increase in error) with a maximum increase in error of 3.9 cm/s. These relatively small changes in the predictions suggest that the nearshore morphology is not the primary mechanism controlling the surf zone hydrodynamics. Instead the large-scale variations caused by the strong refraction patterns over the offshore bathymetry dominate the overall patterns of waves and circulation in the nearshore system. Therefore, unlike many areas of coast where accurate measurements of the nearshore bathymetry (which can change on daily-weekly time scales) are required to generate reliable hydrodynamic model predictions, accurate depiction of the larger scale, permanent offshore features can be sufficient to obtain reasonable hydrodynamic predictions at this site. Certainly, the nearshore bathymetry still plays a role in smaller-scale hydrodynamic variations and model accuracy will improve to some degree when using the most up-to-date data.

With regard to the predicted rip currents, slight differences are present in most of the rip current time series with the most significant discrepancy in the rip current centered around $y = 1500$ m. Interestingly, the simulations performed without updating the nearshore bathymetry exhibit weaker rip currents during regime V (27 October to 30 October) than the original simulations. The rip current magnitude predicted in this simulation is reduced by almost 50% making them more comparable to those observed during regime III. We note that bathymetry measurements collected during the experiment show the growth of a shoal just offshore of where this rip current is predicted indicating that at this location significant sediment transport did occur.

Some previous work has shown that during periods of time following the month-long time series considered here, small alongshore variations (O(25 cm)) in the nearshore bathymetry developed at the northern end of the site (away from the influence of the canyon) [*MacMahan et al*., 2008]. These variations induced a topographic rip current when the incident wave angles were small and the alongshore current magnitude was approximately zero. Without this constraint, *MacMahan et al*. [2008] find that the rip current is not formed. This finding is consistent with the results of *Long and Özkan-Haller* [2005] who found that a rip current does not form when the inertia of the alongshore current exceeds small set-up variations in the surf zone. Note that in our domain, which is highly influenced by wave refraction over the canyon, small angles of incidence are not common.

7. Conclusions

A month-long simulation of the wave and current field along a region with complex bathymetry was performed in order to analyze the dynamics of rip currents dictated primarily by features in the offshore bathymetry for a variety of incident wave conditions. The model was validated using both in situ and remote sensing data and was shown to reasonably reproduce the hydrodynamics observed over this 4 week period. The wave height in the surf zone was consistently over-predicted with ε_{rms} of up to 13 cm at the 1 m isobath, but we observed no appreciable bias in the wave model error as a function of alongshore position in any portion of the domain. Errors in the predicted mean alongshore current were less than 18.5 cm/s for seven out of eight instruments and larger at the current meter just north of the canyon. The observed and predicted mean alongshore current directions compare well suggesting that the model can correctly predict the convergences and divergences of the alongshore current, and therefore rip current positions. Additionally, modeled rip current locations correspond to rip positions observed in remote sensing images during three events.

Modeled quantities were used to define and record rip currents on an hourly basis for the entire month. Time series of the rip current position and magnitude within alongshore regions were constructed to relate with observed wave conditions. Through the analysis, we determined a number of characteristics about the forcing of the nonstationary rip currents observed at this site.

1. An incident wave spectrum dominated by swell waves approaching from the northwest is expected to create strong alongshore variability in wave height forcing multiple strong rip currents in the domain. The rip current strength is related to the magnitude of the incident wave height.
2. The peak period of the incident waves becomes very important under northern wave conditions. As the period decreases, alongshore gradients of wave height in the nearshore are less pronounced. This, in addition

to the inertia of the alongshore current that can overcome small setup gradients, causes all rip currents to be concentrated in the southern portion of the domain. This was first described using idealized cases by *Long and Özkan-Haller* [2005] but confirmed here using observed wave and bathymetric conditions.

3. When incident waves from the southwest dominate the wave spectrum, the number and relative magnitude of rip currents at the site is reduced. This occurs due to changes in wave refraction patterns where one large wave focusing region and adjacent shadow zone is present but smaller scale fluctuations (O(100 m)) are much less pronounced. Hence, a diverging mean alongshore current develops and one or two weak rip currents may be observed.
4. In a bimodal spectrum, the integrated energy in each peak is more diagnostic than identifying the peak spectral direction when determining if strong rip current activity will be generated.
5. Unlike topographic rips, variations in the rip current strength were not correlated with changes in the tidal elevation.
6. The offshore bathymetry, rather than nearshore bathymetric variations, controls the overall flow patterns. While surf zone bathymetry controls the hydrodynamics at many beaches, along this section of coast the wave and circulation dynamics are dominated by offshore bathymetric features, and updating the nearshore bathymetry in the model predictions yields little improvement in model accuracy.
7. Nonlinear processes have a significant impact on the location, persistence, and strength of modeled rip currents.

Acknowledgments

The authors express their gratitude to all researchers involved with the Nearshore Canyon Experiment for their contributions in collecting and processing this valuable data set. In addition, special thanks to Bill O'Reilly and the Coastal Data Information Program (CDIP) for furnishing measurements of and guidance regarding the offshore wave climate. The in situ observations were collected and provided by Steve Elgar and Britt Raubenheimer at the Woods Hole Oceanographic Institution PVLAB and Bob Guza at the Scripps Institution of Oceanography. Rob Holman and the Coastal Imaging Laboratory were responsible for collecting and providing the Argus data. We also thank Tom Lippman for collection of the bathymetric surveys. Jenna Brown, two anonymous reviewers, and the journal editors all provided valuable feedback that improved this paper. This research was sponsored by the Office of Naval Research, Littoral Geosciences and Optics Program under grant N00014-02-1-0198 and the U.S. Geological Survey Coastal and Marine Geology Program. Any use of trade, firm, or product names is for descriptive purposes only and does not imply endorsement by the U.S. Government. Model setup and output from this study can be made available upon request to the corresponding author (jwlong@usgs.gov).

References

Apotsos, A., B. Raubenheimer, S. Elgar, and R. T. Guza (2008a), Wave-driven setup and alongshore flows observed onshore of a submarine canyon, *J. Geophys. Res.*, *113*, C07025, doi:10.1029/2007JC004514.

Apotsos, A., B. Raubenheimer, S. Elgar, and R. T. Guza (2008b), Testing and calibrating parametric wave transformation models on natural beaches, *Coastal Eng.*, *55*(3), 224–235, doi:10.1016/j.coastaleng.2007.10.002.

Battjes, J. A., and J. P. F. M. Janssen (1978), Energy loss and set-up due to breaking random waves, in *Proceedings of 16th International Conference on Coastal Engineering*, pp. 68–81, Am. Soc. of Civ. Eng., N. Y.

Booij, N., R. C. Ris, and L. H. Holthuijsen (1999), A third-generation wave model for coastal regions: 1. Model description and validation, *J. Geophys. Res.*, *104*(C4), 7649–7666.

Bouws, E., H. Gunther, W. Rosenthal, and C. Vincent (1985), Similarity of the wind wave spectrum in finite water depth, *J. Geophys. Res.*, *90*(C1), 975–986.

Brander, R. W. (1999), Field observations on the morphodynamic evolution of a low-energy rip current system, *Mar. Geol.*, *157*, 199–217.

Fowler, R. E., and R. A. Dalrymple (1990), Wave group forced nearshore circulation, in *Proceedings of 22nd International Conference on Coastal Engineering*, edited by Billy J. Edge, pp. 729–742, Am. Soc. of Civ. Eng., N. Y.

Gorrell, L., B. Raubenheimer, S. Elgar, and R. T. Guza (2011), Swan predictions of waves observed in shallow water onshore of complex bathymetry, *Coastal Eng.*, *58*(6), 510–516.

Haller, M. C., R. A. Dalrymple, and Ib A. Svendsen (2002), Experimental study of nearshore dynamics on a barred beach with rip channels, *J. Geophys. Res.*, *107*(C6), 3061, doi:10.1029/2001JC000955.

Hansen, J. E., B. Raubenheimer, J. H. List, and S. Elgar (2015), Modeled alongshore circulation and force balances onshore of a submarine canyon, *J. Geophys. Res. Oceans*, *120*, 1887–1903, doi:10.1002/2014JC010555.

Holman, R. A., and J. Stanley (2007), The history and technical capabilities of Argus, *Coastal Eng.*, *54*, 477–491, doi:10.1016/j.coastaleng.2007.01.003.

Johnson, D., and C. Pattiaratchi (2004), Transient rip currents and nearshore circulation on a swell-dominated beach, *J. Geophys. Res.*, *109*, C02026, doi:10.1029/2003JC001798.

Komar, P. (1998), *Beach Processes and Sedimentation*, 2nd ed., 336–350, Prentice Hall, Upper Saddle River, N. J.

Long, J. W., and H. Tuba Özkan-Haller (2005), Offshore controls on nearshore rip currents, *J. Geophys. Res.*, *110*, C12007, doi:10.1029/2005JC003018.

Long, J. W., and H. Tuba Özkan-Haller (2009), Low frequency characteristics of wave group forced vortices, *J. Geophys. Res.*, *114*, C08004, *doi*:10.1029/2008JC004894.

Longuett-Higgins, M. S., and R. W. Stewart (1964), Radiation stresses in water waves; a physical discussion with applications, *Deep Sea Res. Oceanogr. Abstr.*, *11*, 529–562.

Lygre, A., and H. E. Krogstad (1986), Maximum entropy estimation of the directional distribution in ocean wave spectra, *J. Phys. Oceanogr.*, *16*(12), 2052–2060.

MacMahan, J. H., Ad J. H. M. Reniers, E. B. Thornton, and T. P. Stanton (2004), Infragravity rip current pulsations, *J. Geophys. Res.*, *109*, C01033, doi:10.1029/2003JC002068.

MacMahan, J. H., Ed B. Thornton, T. P. Stanton, and Ad J. H. M. Reniers (2005), Ripex: Observations of a rip current system, *Mar. Geol.*, *218*(1–4), 113–134, doi:10.1016/j.margeo.2005.03.019.

MacMahan, J. H., Ed B. Thornton, and Ad J. H. M. Reniers (2006), Rip current review, *Coastal Eng.*, *53*, 191–208, doi:10.1016/j.coastaleng.2005.10.009.

MacMahan, J. H., Ed. B. Thornton, Ad. J. H. M. Reniers, T. P. Stanton, and G. Symonds (2008), Low-energy rip currents associated with small bathymetric variations, *Mar. Geol.*, *255*, 156–164, doi:10.1016/j.margeo.2008.08.006.

Magne, R., K. A. Belibassakis, T. H. C. Herbers, F. Ardhuin, W. C O'Reilly, and V. Rey (2007), Evolution of surface gravity waves over a submarine canyon, *J. Geophys. Res.*, *112*, C01002, doi:10.1029/2005JC003035.

Özkan-Haller, H. T., and Y. Li (2003), Effects of wave-current interaction on shear instabilities of longshore currents, *J. Geophys. Res.*, *108*(C5), 3139, doi:10.1029/2001JC001287.

Raubenheimer, B., S. Elgar, and R. T. Guza (1998), Estimating wave heights from pressure measured in sand bed, *J. Waterw. Port Coastal Ocean Eng.*, *124*(3), 151–154, doi:10.1061/(ASCE)0733-950X(1998)124:3(151).

Reniers, A. J. H. M., J. A. Roelvink, and E. B Thornton (2004a), Morphodynamic modeling of an embayed beach under wave group forcing, *J. Geophys. Res.*, *109*, C01030, doi:10.1029/2002JC001586.

Reniers, A. J. H. M., E. B. Thornton, T. P. Stanton, and J. A. Roelvink (2004b), Vertical flow structure during Sandy Duck: Observations and modeling, *Coastal Eng.*, *51*, 237–260, doi: 10.1016/j.coastaleng.2004.02.001.

Smith, J. A., and J. L Largier (1995), Observations of nearshore circulation: Rip currents, *J. Geophys. Res.*, *100*(C6), 10,967–10,975.